Black hole accretion discs and jets at super-Eddington luminosity

T. Okuda,[1]★ V. Teresi,[2] E. Toscano[2] and D. Molteni[2]

[1]*Hakodate College, Hokkaido University of Education, Hachiman-cho 1-2, Hakodate 040-8567, Japan*
[2]*Dipartimento di Fisica e Tecnologie Relative, Universita di Palermo, Viale delle Scienza, Palermo 90128, Italy*

ABSTRACT

Super-Eddington accretion discs with $3\dot{M}_E$ and $15\dot{M}_E$ around black holes with mass $10\,M_\odot$ are examined by two-dimensional radiation hydrodynamical calculations extending from the inner disc edge to $5 \times 10^4 r_g$ and lasting up to $\sim 10^6\, r_g/c$. The dominant radiation pressure force in the inner region of the disc accelerates the gas vertically to the disc plane, and jets with 0.2–$0.4c$ are formed along the rotational axis. In the case of the lower accretion rate, the initially anisotropic high-velocity jet expands outward and becomes gradually isotropic flow in the distant region. The mass-outflow rate from the outer boundary is as large as $\sim 10^{19}$–10^{23} g s^{-1}, but it is variable and intermittent with time; that is, the outflow switches occasionally to inflow in the distant region. The luminosity also varies as $\sim 10^{40}$–10^{42} erg s^{-1} on a long time-scale. On the other hand, the jet in the case of the higher accretion rate maintains its initial anisotropic shape even after it goes far away. The mass-outflow rate and the luminosity attain steady values of 3×10^{19} g s^{-1} and 1.3×10^{40} erg s^{-1}, respectively. In accordance with the local analysis of the slim accretion disc model, the disc is thermally unstable in the case of $3\dot{M}_E$ but stable in the case of $15\dot{M}_E$. The super-Eddington model with $15\dot{M}_E$ promises to explain the small collimation degree of the jet and the large mass-outflow rate observed in the X-ray source SS 433.

Key words: accretion, accretion discs – black hole physics – hydrodynamics – radiation mechanisms: thermal – X-rays: individual: SS 433.

1 INTRODUCTION

Disc accretion is an essential process for dynamic phenomena such as energetic X-ray sources, active galactic nuclei and protostars. Since the early work by Pringle & Rees (1972) and Shakura & Sunyaev (1973), a great number of papers have been devoted to studies of disc accretion on to gravitating objects, and the standard accretion disc models with a geometrically thin disc have proven to be particularly successful in applications to cataclysmic variables. However, for very luminous accretion discs whose luminosity exceeds the Eddington luminosity, we need another disc model instead of the standard model because the disc is expected to have a geometrically thick structure and powerful outflows from the disc. It is well known that luminous accretion discs, where radiation pressure and electron scattering are dominant, are thermally unstable if the usual α-model for the viscosity is used. For a luminous disc, the slim accretion disc model has been proposed by Abramowicz et al. (1988), where strong advective cooling depresses the thermal instability. The slim-disc model seems to be reasonable for accretion discs at the super-Eddington luminosity, but we need to reconfirm it from the point of view of a two-dimensional simulation. Super-

Eddington accretion discs were generally expected to possess vortex funnels and radiation pressure driven jets from geometrically thick discs (Shakura & Sunyaev 1973; Lynden-Bell 1978; Fukue 1982). A two-dimensional hydrodynamical calculation of a super-Eddington accretion disc around a black hole was first examined by Eggum, Coroniti & Katz (1985, 1988), and was discussed regarding SS 433. Although they showed relativistic jet formation just outside a conical photosphere of the accretion disc and a collimation angle of $\sim 30°$ of the jet, the mass flux of the jet is too small and the collimation angle is much larger than the one observed for SS 433.

Blandford & Begelman (1999) investigated an adiabatic inflow–outflow solution of the accretion disc, where the super-Eddington flow leads to a powerful wind. King & Begelman (1999) discussed the super-Eddington mass transfer in binary systems and how to accrete in such super-Eddington accretion discs. Recent theoretical studies and two-dimensional simulations of black hole accretion flows (Igumenshchev & Abramowicz 1999; Stone, Pringle & Begelman 1999; Narayan, Igumenshchev & Abramowicz 2000; Quataert & Gruzinov 2000; Abramowicz & Igumenshchev 2001; Stone & Pringle 2001) showed a new development in advection-dominated accretion flows (ADAFs) and convection-dominated accretion flows (CDAFs) which may be deeply related to super-Eddington accretion flows. Furthermore, from a point of view completely different from the α-viscosity models for accretion

★E-mail: okuda@cc.hokkyodai.ac.jp

discs, recently developed rigorous investigations with global three-dimensional magnetohydrodynamic (MHD) simulations of black hole accretion flows should be noted (Hawley & Balbus 2002; Balbus & Hawley 2003). They show that, without the assumption of the phenomenological α-viscosity, magnetic fields play the most important role in angular momentum transport; that is, accretion is driven by turbulent stresses generated self-consistently by the magnetorotational instability. The results reveal a three-component structure: a warm Keplerian disc, a highly magnetized corona, and an axial jet.

Okuda (2002) examined the super-Eddington black hole model for SS 433 based on two-dimensional hydrodynamical calculations coupled with radiation transport. Although, in this model, a high-velocity jet with 0.2–0.4c is formed along the rotational axis, the small collimation angle of $\sim$0.1 radian of the jets and a sufficient mass-outflow rate comparable to $\sim 10^{19}$ g s^{-1} could not be obtained. Additionally, it was also suggested that this result might be transient behaviour during a long disc evolution (Teresi, Molteni & Toscano 2004). Keeping these facts in mind, we further examine super-Eddington accretion discs and jets around the black hole extending from the inner disc edge to 5×10^4 r_g.

2 MODEL EQUATIONS

A set of relevant equations consists of six partial differential equations for density, momentum, and thermal and radiation energy. These equations include the full viscous stress tensor, heating and cooling of the gas, and radiation transport. The radiation transport is treated in the grey, flux-limited diffusion approximation (Levermore & Pomraning 1981). We use spherical polar coordinates (r, ζ, φ), where r is the radial distance, ζ is the polar angle measured from the equatorial plane of the disc, and φ is the azimuthal angle. The gas flow is assumed to be axisymmetric with respect to the Z-axis ($\partial/\partial \varphi = 0$) and the equatorial plane. In this coordinate system, the basic equations for mass, momentum, gas energy, and radiation energy are written in the following conservative form (Kley 1989):

$$\frac{\partial \rho}{\partial t} + \mathrm{div}(\rho v) = 0, \tag{1}$$

$$\frac{\partial(\rho v)}{\partial t} + \mathrm{div}(\rho v v) = \rho \left[\frac{w^2}{r} + \frac{v_\varphi^2}{r} - \frac{GM_*}{(r - r_g)^2} \right]$$
$$- \frac{\partial p}{\partial r} + f_r + \mathrm{div}\, S_r + \frac{1}{r} S_{\mathrm{rr}}, \tag{2}$$

$$\frac{\partial(\rho r w)}{\partial t} + \mathrm{div}(\rho r w v) = -\rho v_\varphi^2 \tan \zeta - \frac{\partial p}{\partial \zeta} + \mathrm{div}(r S_\zeta)$$
$$+ S_{\varphi\varphi} \tan \zeta + f_\zeta, \tag{3}$$

$$\frac{\partial(\rho r \cos \zeta\, v_\varphi)}{\partial t} + \mathrm{div}(\rho r \cos \zeta\, v_\varphi v) = \mathrm{div}(r \cos \zeta\, S_\varphi), \tag{4}$$

$$\frac{\partial \rho \varepsilon}{\partial t} + \mathrm{div}(\rho \varepsilon v) = -p\, \mathrm{div}\, v + \Phi - \Lambda, \tag{5}$$

and

$$\frac{\partial E_0}{\partial t} + \mathrm{div}\, F_0 + \mathrm{div}(v E_0 + v \cdot P_0) = \Lambda - \rho \frac{(\kappa + \sigma)}{c} v \cdot F_0, \tag{6}$$

where ρ is the density, $v = (v, w, v_\varphi)$ are the three velocity components, G is the gravitational constant, M_* is the central mass, p is the gas pressure, ε is the specific internal energy of the gas, E_0 is the radiation energy density per unit volume, and P_0 is the radiative stress tensor. The subscript '0' denotes the value in the comoving

frame and that the equations are correct to first order in v/c (Kato, Fukue & Mineshige 1998). We adopt the pseudo-Newtonian potential (Paczynsky & Wiita 1980) in equation (2), where r_g is the Schwarzschild radius. The force density $f_R = (f_r, f_\zeta)$ exerted by the radiation field is given by

$$f_R = \rho \frac{\kappa + \sigma}{c} F_0, \tag{7}$$

where κ and σ denote the absorption and scattering coefficients and F_0 is the radiative flux in the comoving frame. For the opacities κ we use polynomial fits to the Rosseland mean opacities given by Lin & Papaloizou (1985). $S = (S_r, S_\zeta, S_\varphi)$ denotes the viscous stress tensor which includes all components due to the three velocity components (Okuda, Fujita & Sakashita 1997). $\Phi = (S \nabla)\, v$ is the viscous dissipation rate per unit mass.

The quantity Λ describes the cooling and heating of the gas,

$$\Lambda = \rho c \kappa (S_* - E_0), \tag{8}$$

where S_* is the source function and c is the speed of light. For this source function, we assume local thermal equilibrium $S_* = aT^4$, where T is the gas temperature and a is the radiation constant. For the equation of state, the gas pressure is given by the ideal gas law, $p = R_G \rho T/\mu$, where μ is the mean molecular weight and R_G is the gas constant. The temperature T is proportional to the specific internal energy, ε, given by the relation $p = (\gamma - 1)\rho\varepsilon = R_G \rho\, T/\mu$, where γ is the specific heat ratio. To close the system of equations, we use the flux-limited diffusion approximation (Levermore & Pomraning 1981) for the radiative flux:

$$F_0 = -\frac{\lambda c}{\rho(\kappa + \sigma)} \mathrm{grad}\, E_0, \tag{9}$$

and

$$P_0 = E_0 \cdot T_{\mathrm{Edd}}, \tag{10}$$

where λ and T_{Edd} are the flux limiter and the Eddington tensor, respectively, for which we use the approximate formulae given in Kley (1989). The formulae fulfil the correct limiting conditions in the optically thick diffusion limit and the optically thin streaming limit, respectively.

For the kinematic viscosity, ν, we adopt a modified version (Papaloizou & Stanley 1986) of the standard α-model. The modified prescription for ν is given by

$$\nu = \alpha\, c_s \min[H_p, H], \tag{11}$$

where α is a dimensionless parameter, c_s the local sound speed, and H the disc height. $H_p = p/|\mathrm{grad}\, p|$ is the mid-plane pressure scale-height inside of the disc but the local pressure scaleheight outside of the disc.

3 NUMERICAL METHODS

The set of partial differential equations (1)–(6) is numerically solved by a finite-difference method under adequate initial and boundary conditions. The numerical schemes used are basically the same as that described by Kley (1989) and Okuda et al. (1997). The methods are based on an explicit–implicit finite difference scheme. Grid points in the radial direction are spaced logarithmically as $\Delta r/r = 0.1$, while grid points in the angular direction are equally spaced, but more refined near the equatorial plane, typically $\Delta \zeta = \pi/150$ for $\pi/2 \geqslant \zeta \geqslant \pi/6$ and $\Delta \zeta = \pi/300$ for $\pi/6 \geqslant \zeta \geqslant 0$. Although the radial mesh-sizes do not have a fine resolution to examine detailed disc structure, we consider the mesh-sizes to be sufficient for examination of the global behaviour of the disc, the jet, and the mass-outflow rate, as is later shown in Section 4.2.

Table 1. Model parameters.

Model	$\dot{m}$	$\dot{M}(\text{ g s}^{-1})$	$R_{\max}/r_{\mathrm{g}}$	L/L_{E}	$\dot{M}_{\mathrm{out}}/\dot{M}$	$\dot{M}_{\mathrm{in}}/\dot{M}$
1	3	8×10^{19}	5×10^4	variable	variable	0.4
2	15	4×10^{20}	5×10^4	8	0.08	0.2

3.1 Model parameters

We consider a Schwarzschild black hole with mass $M_* = 10 \, \mathrm{M_{\odot}}$ and take the inner boundary radius R_{in} of the computational domain as $2r_{\mathrm{g}}$. The model parameters used are listed in Table 1, where $R_{\max}$ is the outer boundary radius, and $\dot{m}$ is the input accretion rate normalized to the Eddington critical accretion rate $\dot{M}_{\mathrm{E}}$ which is given by

$$\dot{M}_{\mathrm{E}} = 16L_{\mathrm{E}}/c^2, \tag{12}$$

where L_{E} is the Eddington luminosity. L, $\dot{M}_{\mathrm{out}}$ and $\dot{M}_{\mathrm{in}}$ in Table 1 denote the total luminosity through the outer boundary surface, the mass-outflow rate ejected from the outer boundary, and the mass-inflow rate swallowed into the black hole through the inner boundary at the final state. The viscosity parameter $\alpha = 10^{-3}$ is adopted, since in the previous examination we found that the low value of $\alpha = 10^{-3}$ is more advantageous for the formation of the collimated high-velocity jets than the high-value case with $\alpha = 0.1$ (Okuda 2002).

3.2 Initial conditions

The initial conditions consist of a cold, dense and optically thick disc and a hot, rarefied and optically thin atmosphere around the disc. The initial disc at $r/r_{\mathrm{g}} \geqslant 3$ is approximated by the Shakura–Sunyaev standard model but, at $2 \leqslant r/r_{\mathrm{g}} \leqslant 3$, it is taken to be a sub-Keplerian disc with a free-fall velocity at the inner boundary. To examine how the high-velocity jet evolves through the surrounding matter, it is important, for us, to set up the appropriate density distribution around the disc. Observations and hydrodynamical modelling of the SS 433 jet (Kotani et al. 1996) suggest that the X-ray emitting region of SS 433 would be in the range of $r = 10^{10}$–10^{12} cm from the central source and have gas densities of $\sim 10^{-12}$–$10^{-10} \, \mathrm{g \, cm^{-3}}$ at the base of the X-ray jets. Focusing on these facts, we take the density at the outer boundary radius of 1.5×10^{11} cm to be $\sim 10^{-14} \, \mathrm{g \, cm^{-3}}$. Furthermore, assuming the density distribution of $\rho \sim r^{-1}$, we construct an initial hot rarefied atmosphere around the disc to be approximately in radial hydrostatic equilibrium.

3.3 Boundary conditions

Physical variables at the inner boundary, except for the velocities, are given by extrapolation of the variables near the boundary. However, we impose limited conditions that the radial velocities are given by a free-fall velocity and the angular velocities are zero. On the rotational axis and the equatorial plane, the meridional tangential velocity w is zero and all scalar variables must be symmetric relative to these axes. The outer boundary at $r = R_{\max}$ is divided into two parts. One is the disc boundary through which matter is entering from the outer disc. At the outer disc boundary we assume a continuous inflow of matter with a constant accretion rate $\dot{M}$. The other is the outer boundary region above the accretion disc. We impose free-floating conditions on this outer boundary and allow for outflow of matter, whereas any inflow is prohibited here. We also assume the

outer boundary region above the disc to be in the optically thin limit, $|\boldsymbol{F}_0| \to cE_0$.

4 NUMERICAL RESULTS

### 4.1 The case of $\dot{M} = 3\dot{M}_{\mathrm{E}}$

Model 1 with $\dot{M} = 3\dot{M}_{\mathrm{E}}$ has the same input accretion rate as BH-1 in the previous disc model (Okuda 2002), but the computational domain used is two orders of magnitude larger than the previous one. This is due to the following reasons. We use the initial discs based on the Shakura–Sunyaev model. In the super-Eddington accretion regime, the initial conditions should be carefully used in the treatment of the outer disc boundary, because we do not know a priori reasonable conditions of the very luminous and thick disc. However, if the outer boundary radius is taken to be very large, this problem will be avoidable because the outermost disc is well described by the Shakura–Sunyaev model. Another reason is due to the requirement that we want to examine the behaviour of the high-velocity jet over a distant region, which is observed in the X-ray source SS 433.

The initial disc used is geometrically thick as $H/r \sim 1$ in the inner region, but the relative disc height H/r and the ratio β of the gas pressure to the total pressure are ~ 0.05–0.1 and ~ 0.95–0.98, respectively, at the outer disc boundary for models 1 and 2.

Fig. 1 shows the time evolution of the total luminosity L emitted from the outer boundary surface, the disc luminosity L_{d} emitted from the disc surface, the mass-outflow rate $\dot{M}_{\mathrm{out}}$ from the outer boundary, and the mass-inflow rate $\dot{M}_{\mathrm{in}}$ swallowed into the black hole through the inner boundary for model 1. From the luminosity curve, we can see three characteristic stages: stage 1 ($t = 0$–$2.5 \times 10^5 r_{\mathrm{g}}/c$), stage 2 ($t = 2.5$–$5.5 \times 10^5 r_{\mathrm{g}}/c$), and stage 3 ($t \geqslant 5.5 \times 10^5 r_{\mathrm{g}}/c$). At stage 1, matter in the inner region of the disc is ejected strongly outward and propagates vertically to the disc plane. The high-velocity jet with a velocity of $\sim 0.2c$ reaches the outer boundary in the polar direction at $t \sim R_{\max}/0.2c \sim 2.5 \times 10^5 \, r_{\mathrm{g}}/c$, and then the mass outflow through the outer boundary begins, and the total luminosity L attains
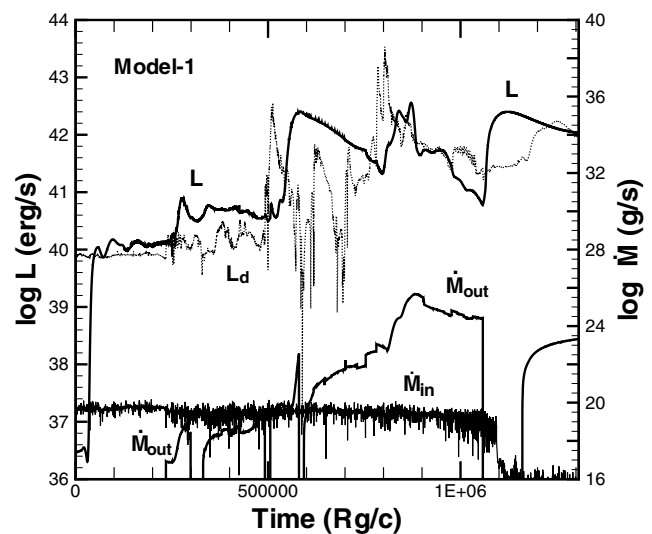
Figure 1. Time evolution of total luminosity L emitted from the outer boundary surface, disc luminosity L_{d} from the disc surface, mass-outflow rate $\dot{M}_{\mathrm{out}}$ from the outer boundary, and mass-inflow rate $\dot{M}_{\mathrm{in}}$ swallowed into the black hole through the inner boundary for model 1, where time is shown in units of r_{g}/c.
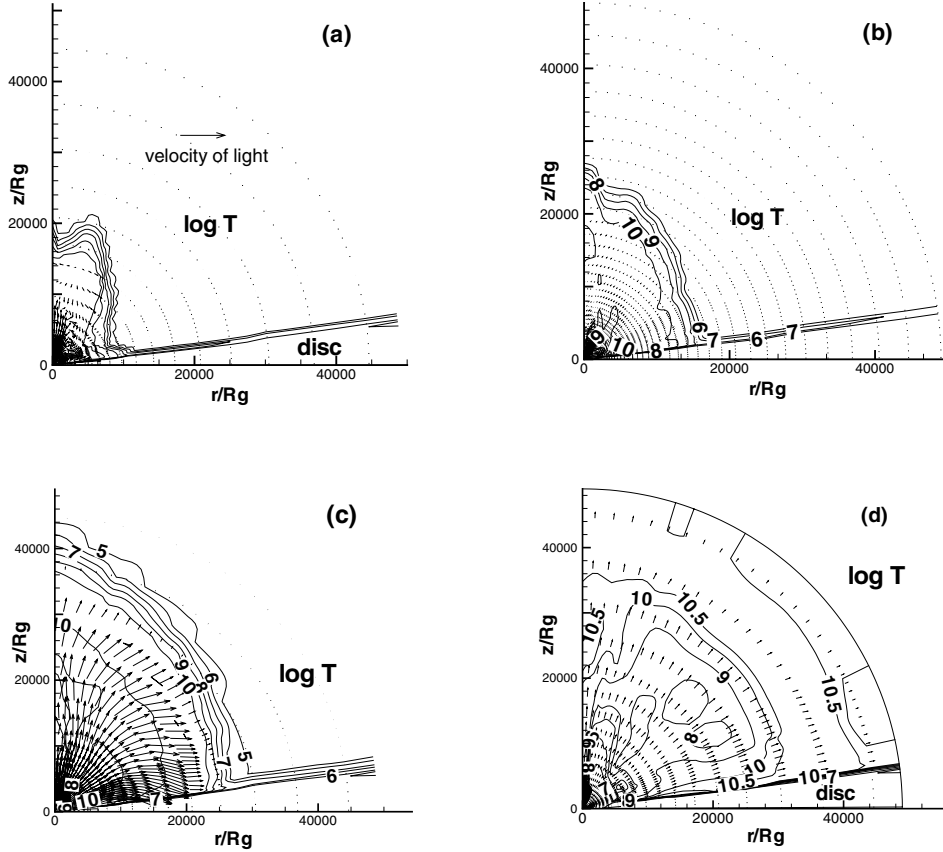
Figure 2. Velocity vectors and temperature contours in logarithmic scale on the meridional plane at $t = 6 \times 10^4$ (a), 1.5×10^5 (b), 2.5×10^5 (c), 2.8×10^5 r_g/c (d) for model 1. The contour lines with labels $\log T = 5, 6, 7, 8, 9, 10$ and 10.5 are shown. The reference vector of light is shown by a long arrow in (a). The initially anisotropic high-velocity jet (a) generated in the inner region of the disc evolves into the isotropic outflow (d) in the distant region. The label 'disc' in the figure denotes the cold and dense accretion disc.

$\sim 10^{40}$ erg s^{-1}. At stage 2, the luminosity flares up to $\sim 4 \times 10^{40}$ erg s^{-1} and maintains its high value for a time of $3 \times 10^5 r_g/c$ and switches to stage 3, flaring up by more than one order of magnitude. During stage 3, the luminosity shows quasi-periodic variations with a period of $2.5 \times 10^5 r_g/c$ and an amplitude of factor 10. Through these stages, the mass-outflow rate $\dot{M}_{\rm out}$ becomes as high as $\sim 10^{19}$–10^{23} g s^{-1}, but it is variable and intermittent as found in Fig. 1; that is, the outflow switches occasionally to inflow. The mass-inflow rate $\dot{M}_{\rm in}$ fluctuates rapidly, but the averaged rate is constantly $\sim 3 \times 10^{19}$ g s^{-1} except in the final phases, where $\dot{M}_{\rm in}$ becomes very small at $\sim 10^{16}$ g s^{-1}. In model 1, the heating wave (see Fig. 7 below) and the density wave, which is generated initially in the innermost disc region, propagate outward with time and reach the outer disc region of $r \sim 3 \times 10^4 r_g$ at $t \sim 1.1 \times 10^6 r_g/c$. In these phases, part of the wave begins to back inward as an ingoing wave, and gradually the ingoing density wave leads to a lower density in the inner disc region and consequently to a smaller mass-inflow rate at the inner boundary.

L and L_d are given by calculating $\int \mathbf{F}_0 \, d\mathbf{S}$, where the surface integral is taken over the outer boundary surface and the disc surface, respectively. Although it is difficult for us to specify correctly the disc surface in the geometrically thick disc, we define it here as the location where the density drops to a tenth of the central density on the equatorial plane. This may lead to some errors in estimation of the disc surface and accordingly L_d. The complicated features of L_d during stage 3 in Fig. 1 may be due to unreliable determinations

of the disc surface. If the atmosphere above the disc is optically thin, L_d must agree with L. L_d has an initial value of $\sim 8 \times 10^{39}$ erg s^{-1} derived from the Shakura–Sunyaev model, while L is initially small and becomes comparable to L_d in the phase $t \sim R_{\rm max}/c = 5 \times 10^4 r_g/c$ when radiation from the disc reaches the outer boundary radius. After $t \sim 2.5 \times 10^5 r_g/c$, the disc luminosity L_d rises to $\sim 1.3 \times 10^{40}$ erg s^{-1} and fluctuates around this value by a factor of 2 during a time of $2.5 \times 10^5 r_g/c$, and then increases sharply to 3×10^{42} erg s^{-1}. The total luminosity L also shows the same behaviour as the disc luminosity but with a phase lag of $5 \times 10^4 r_g/c$, which is the radiation transit time from the disc surface to the outer boundary radius. This time-dependent behaviour of the luminosities is discussed later in terms of the thermal instability of the slim disc.

Fig. 2 shows the temperature contours with velocity vectors at $t = 6 \times 10^4$, 1.5×10^5, 2.5×10^5 and 2.8×10^5 r_g/c in stage 1 for model 1. The evolutionary features of outward moving jets are found here, where the outermost crowded contours of temperature show the shocked region due to the interaction of the jet with the surrounding gas, and the reference velocity of light is indicated by a long arrow in Fig. 2(a). The temperatures are as high as $\sim 10^8$–10^{10} K in the high-velocity region and 'disc' in the figure denotes the cold and dense disc. The initially anisotropic jet (a) propagates vertically to the disc plane but gradually loses its anisotropic nature with increasing time, and finally the jet becomes isotropic flow (d) after the jet reaches the outer boundary. The figure also shows that
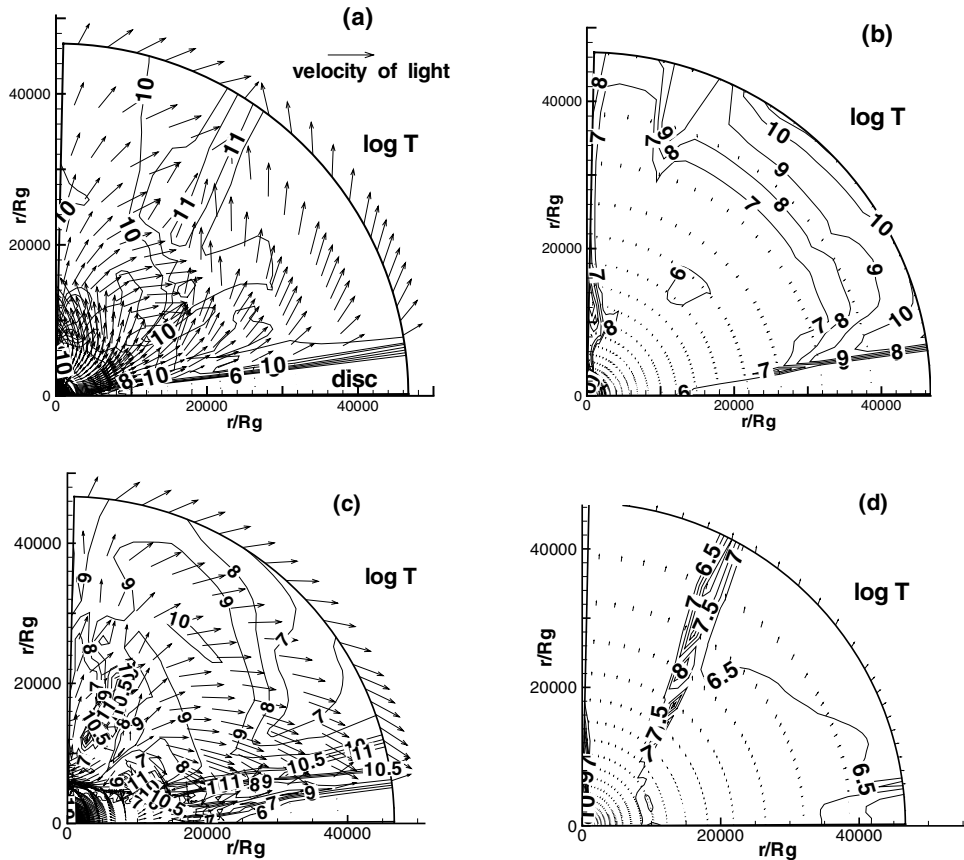
Figure 3. Same as Fig. 2 but at $t = 5.1 \times 10^5$ (a), 5.9×10^5 (b), 8.0×10^5 (c), 1.1×10^6 (d) r_g/c for model 1. (a) and (c) show active outflows in the high-temperature state, but (b) and (d) show inflows (no mass outflow) in the low-temperature state.

there exist an inactive phase (b) and an active phase (c) of outflows. Fig. 3 shows the temperature contours with velocity vectors at $t = 5.0 \times 10^5$, 5.9×10^5, 8.0×10^5 and 1.1×10^6 r_g/c in stage 3. Figs 3(a) and (c) show powerful outflows in the high-temperature state above the disc, whereas Figs 3(b) and (d) show inflow states in the low-temperature state. The inactive inflow states, accompanying with no mass loss, are likely to occur after a large flare-up of the luminosity.

As found in Figs 2 and 3, the gas temperatures in the outflow region outside of the disc are locally too high, at $\sim 10^9$–10^{11} K. These temperatures may be unreliable because we did not take account of other physical processes, such as Compton processes and pair production–annihilation, which would be important at such high temperatures. As far as the disc is concerned, however, the temperatures are in the range $10^6 \leqslant T < 10^8$ K.

4.2 The case of $\dot{M} = 15\dot{M}_E$

The time evolution of L, L_d, $\dot{M}_{out}$ and $\dot{M}_{in}$ for model 2 is shown in Fig. 4. In the initial phases, the disc luminosity L_d and the mass-inflow rate $\dot{M}_{in}$ are very dependent on the initial structure of the inner disc and they fluctuate greatly, but they settle to their steady state values in a time-scale of $\sim 2 \times 10^4$ r_g/c. The total luminosity L becomes comparable to the disc luminosity L_d at $t \sim R_{max}/c = 5 \times 10^4$ r_g/c when radiation from the disc arrives at the outer boundary, and finally it accords with L_d. On the other hand, after $t \sim R_{max}/0.4c = 10^5 r_g/c$, which is the jet transit time from the disc to the outer boundary, the mass outflow begins and $\dot{M}_{out}$ gradually settles down
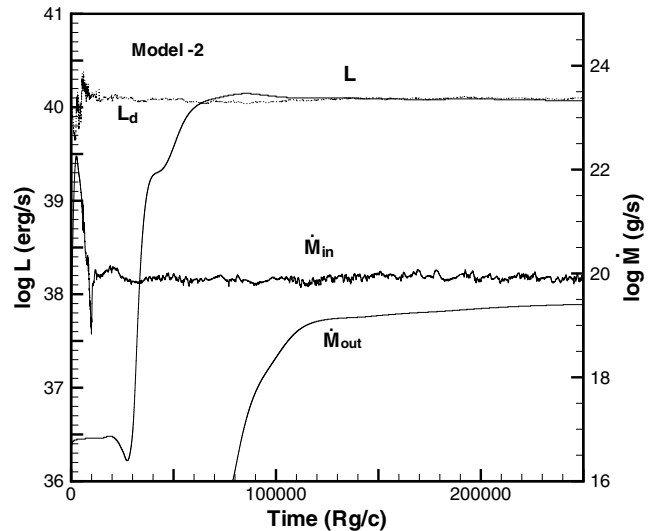
Figure 4. Time evolution of total luminosity L, disc luminosity L_d, mass-outflow rate $\dot{M}_{out}$ from the outer boundary, and mass-inflow rate $\dot{M}_{in}$ swallowed into the black hole through the inner boundary for model 2.

to a steady state value of 3×10^{19} g s^{-1}. Finally, $L = L_d = 1.3 \times 10^{40}$ erg s^{-1}. The mass-inflow rate swallowed into the black hole always fluctuates by a small factor around 8×10^{19} g s^{-1}.

Fig. 5 shows the evolutionary features of the high-velocity jet at $t = 5 \times 10^4$ (a), 8×10^4 (b), 1.5×10^5 (c), and 2.5×10^5 (d). The
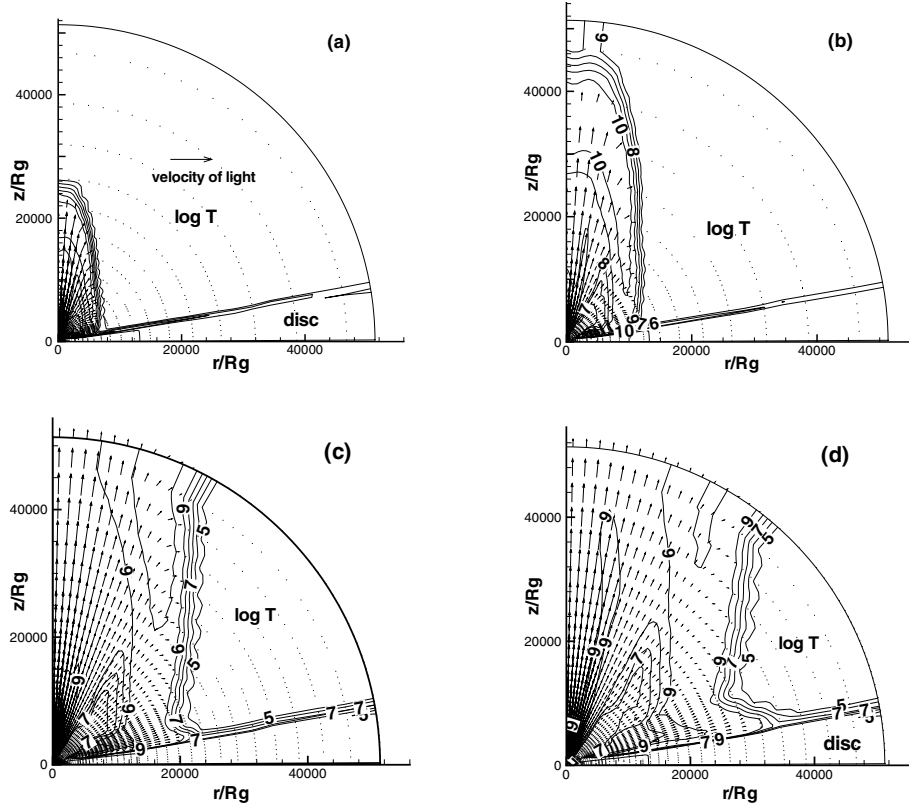
Figure 5. Velocity vectors and temperature contours in logarithmic scale on the meridional plane at $t = 5 \times 10^4$ (a), 8×10^4 (b), 1.5×10^5 (c), 2.5×10^5 (d) but for model 2. Differently from model 1, the initially anisotropic high-velocity jet along the rotational axis maintains its anisotropic shape when it expands outward.

high-velocity jet propagates vertically to the disc plane in the same way as model 1. The jet expands gradually far from the rotational axis with increasing time. After the phase in Fig. 5 (b), the jet arrives at the outer boundary in the polar direction but the anisotropic nature of the jet remains even after it passes through the outer boundary. If the shapes of the jets found in Figs 5 (a) and (b) are always kept throughout the time evolution, we can expect a small collimation angle of $\leqslant 10°$ for the jet.

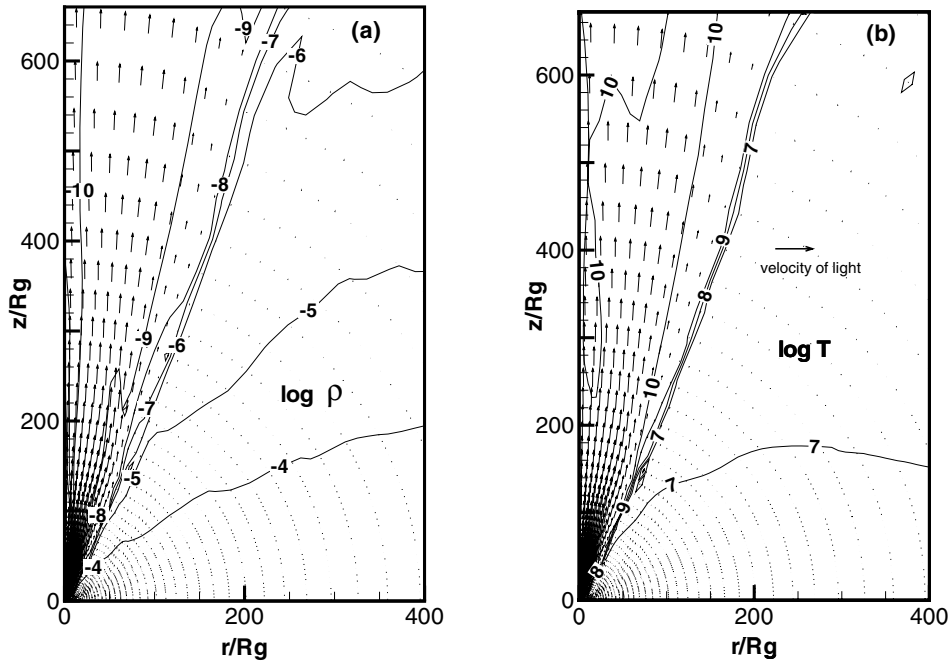Fig. 6 shows the velocity vectors and the contours of density ρ (g cm^{-3}) and temperature T (K) of the disc and the high-velocity jet in the inner region at $t = 2.5 \times 10^5 \, r_g/c$ for model 2. This shows a rarefied, hot, and optically thin high-velocity jet region and a dense, cold, and geometrically thick disc region. The high-velocity region and the disc region are bounded by the funnel wall, a barrier where the effective potential due to the gravitational potential and the centrifugal potential vanishes. The jet velocity in the funnel region between the funnel wall and the Z-axis amounts to $\sim 0.3c$. In the inner disc, the flow is convectively unstable. In the innermost region of the disc, there exist an inner advection-dominated zone and an outer convection-dominated zone. The transition radius r_{tr} between the two zones is approximately $10 \, r_g$. At $r \geqslant r_{tr}$, roughly half the mass at any time at any radius is flowing in and flowing out, respectively, and the mass-inflow rate balances the mass-outflow rate. Near to the transition region, by way of the convective zones and the accretion zone, matter is accreted towards the equatorial plane. The accreting matter, which is carried to the transition by convection, partly diverts into the high-velocity region and partly flows into the inner advection-dominated zone. The gas diverging into the optically thin high-velocity region is originally subsonic but is soon accelerated by the strong radiation field up to a relativistic

velocity. These features of the accreting and outflow materials in the inner region are also found in model 1, even when it is at an inflow phase in the outer region.

In Fig. 6, we see that at the disc boundary the densities lie between label -6 and -7 and a temperature of $\sim 10^7$ K in the disc jumps to $\sim 10^8$ K across the disc boundary. The opening angle of the high-velocity jet to the Z-axis is $\sim 30°$. These density and temperature profiles, the jet velocity, and the opening angle show good agreement with those in the previous calculation extending to $400 \, r_g$ (Okuda 2002), where the relative radial mesh of $\Delta r/r = 0.03$ is finer than 0.1 in the present one but the mesh-sizes in the angular direction have the same resolution. Therefore, the present results over an extended region of $\sim 5 \times 10^4 \, r_g$ are considered to be also valid in spite of the coarse radial mesh-sizes.

The disc and the jet in model 2 attain almost steady states, while model 1 shows variable luminosities and non-steady gas flows. This behaviour of the disc luminosity in models 1 and 2 is considered in terms of the thermal instability of the slim accretion disc model. The thermal instability of the standard disc is interpreted by the relation between the accretion rate $\dot{m}$ and the surface density Σ at a fixed radius r. When the curve of $\dot{m} = \dot{m}(\Sigma)$ has a characteristic S-shape with three branches (lower, middle and upper), the discs in the upper and lower branches are stable against thermal instability, but in the middle branch the disc is unstable. If the disc is under the unstable middle branch, it is expected that the disc exhibits a limit-cycle behaviour of luminosity.

Taking account of advective cooling, Abramowicz et al. (1988) found the S-shaped $\dot{m}-\Sigma$ curve at $r = 5r_g$, corresponding to moderately super-Eddington accretion rates from the transonic solutions of a black hole with $M_* = 10 \, M_{\odot}$ and $\alpha = 10^{-3}$. According to their
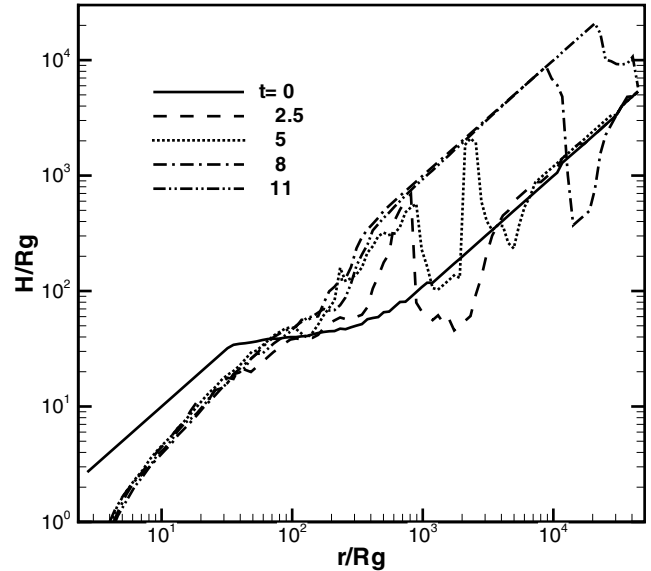
Figure 6. Velocity vectors and contours of density (a) and temperature (b) in the inner region of the disc and the high-velocity jet at $t = 2.5 \times 10^5$ for model 2. The contour labels denote the logarithmic values of the density ρ (g cm^{-3}) and the temperature T (K).
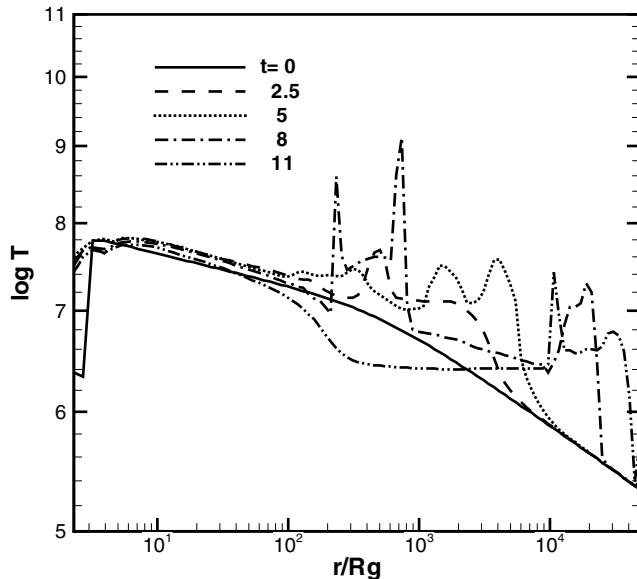
Figure 7. Temperature versus radius on the equatorial plane at $t = 0$ (line), 2.5×10^5 (dashed line), 5.1×10^5 (dotted line), 8.0×10^5 (dash-dot line) and 1.1×10^6 (dash-dot-dot line) $r_{\rm g}/c$ for model 1.

Figure 8. Disc height H versus radius on the equatorial plane at $t = 0$ (line), 2.5×10^5 (dashed line), 5.1×10^5 (dotted line), 8.0×10^5 (dash-dot line) and 1.1×10^6 (dash-dot-dot line) $r_{\rm g}/c$ for model 1.

results, the inner disc with $\dot{m} = 15$ in our model 2 corresponds to the stable upper branch, while the disc with $\dot{m} = 3$ belongs marginally to the unstable middle branch and is located near the turning point between the upper and middle branches. Fig. 7 denotes the temperature versus radius on the equatorial plane at $t = 0$, 2.5×10^5, 5.1×10^5, 8.0×10^5 and 1.1×10^6 $r_{\rm g}/c$ for model 1. The maximum luminosity appears at $t = 5.1 \times 10^5$ $r_{\rm g}/c$. The evolution of the disc temperature is qualitatively similar to the results by Honma, Matsumoto & Kato (1991) and Szuszkiewicz & Miller (1998), who found a limit-cycle behaviour of the slim disc with $\dot{m} = 0.06$ and

$\alpha = 0.1$ by one-dimensional calculations of vertically integrated equations. The model with $\dot{m} = 0.06$ and $\alpha = 0.1$, which belongs to the unstable middle branch of the $\dot{m}$–Σ curve at $r/r_{\rm g} = 5$, is located just near another turning point between the unstable middle branch and stable lower branches. In their results, the outgoing heating wave reaches about $100 r_{\rm g}$, while in ours the heating wave attains $\sim 3 \times 10^4$ $r_{\rm g}$. The disc height H versus radius in the same phases as Fig. 7 is shown in Fig. 8. In the initial phase, H/r is ~ 0.1 at $r/r_{\rm g} \geqslant 10^3$, but the outgoing heating wave leads to $H/r \sim 1$ in the outer disc region and the radiation pressure is dominant there.

Compared with the results by Honma et al. (1991) and Szuszkiewicz & Miller (1998), the heating wave reaches the extensively distant region because of the much higher input accretion rate used. Apart from the effects due to the much higher accretion rate, we can see similar characteristics of the disc evolution between theirs and us and expect a limit cycle behaviour of the luminosity in model 1. However, in order to confirm the limit cycle phenomenon of the luminosity, the computational time in model 1 may not be sufficient because the temperature evolution shows only the phases of the outgoing heating wave.

On the other hand, the super-Eddington disc with $\dot{m} = 15$ is stable against the thermal instability due to the strong advective cooling. In this model, an outgoing heating wave with temperatures of 10^8 K $\leqslant T \leqslant 10^{10}$ K is generated near the inner edge of the disc at the initial phases and reaches about $\sim 10^2 \, r_{\mathrm{g}}$. However, these waves fade out soon and successively the second heating wave generates near the inner edge and oscillates at $2 \leqslant r/r_{\mathrm{g}} \simeq 10$ during a time of $\sim 10^4 \, r_{\mathrm{g}}/c$, and finally they are stabilized completely.

5 COMPARISON WITH SS 433

SS 433 is a typical stellar black hole candidate at a highly super-Eddington luminosity. Our results may be compared with the observations in SS 433. The observations show many emission lines of heavy elements, such as Fe and Ni, which denote the unique red and blue Doppler shifts of $0.26 \, c$ in the X-ray region. The collimation angle of the SS 433 jets seems to be as small as 0.1 radian (several degrees). From an observational constraint of the mass-outflow rate, Kotani et al. (1996) shows $\dot{M}_{\mathrm{out}} \geqslant 3 \times 10^{19} \mathrm{g \, s^{-1}}$ in SS 433.

The unique velocity, $0.26 \, c$, may be reasonably explained in terms of the relativistic velocities accelerated by the radiation pressure force in the inner region of the super-Eddington disc. In our models, the collimation degree of the high-velocity jets will be dependent on the initial density distribution of the matter around the disc. However, the density distribution used is not a special type of profile but the usual spherical one with $\rho \propto r^{-1}$. In model 1, the initial jet is strongly collimated in the polar region, but it becomes isotropic flow in the distant region of $\sim 10^{11}$ cm, where the X-ray jet is observed in SS 433. In model 2 the small collimation angle of the jet is maintained throughout the jet propagation. If the anisotropic nature of the jet found in Figs 5 (a) and (b) is maintained throughout the disc evolution, it is expected that the collimation angle of the jet is as small as $\leqslant 10°$. Furthermore, in addition to models 1 and 2, we examined the intermediate case with $\dot{m} = 10$ between them and found that the case also shows the same anisotropic outflows as model 2 but with a smaller collimation angle than that in model 2. From these results, we speculate that the collimation angle may be smaller if we consider other models with much higher input accretion rates. This should be confirmed in the future. Of course, axisymmetric MHD disc simulations have been used successfully in the past to reproduce jet formation and collimation of the jets since Shibata & Uchida (1986), and the recent 3D MHD simulations, which have been directed at the internal dynamics of the disc itself and the resulting accretion flow, also show an unbound outflowing jet along the *Z*-axis confined by magnetic pressure. However, as far as the very luminous X-ray source SS 433 is concerned, the jet acceleration is considered to be mainly of thermal origin instead of magnetic origin. Therefore it is very advantageous for us to be able to reproduce a small collimation angle of the jet in terms of the thermal model considered here.

The mass-outflow rate in model 1 is as large as $\sim 10^{19}$–10^{23} g s^{-1} but is variable and intermittent with time, while in model 2 it is as large as $\sim 3 \times 10^{19}$ g s^{-1}, and it is stable, and comparable to the mass-outflow rate estimated in SS 433.

6 CONCLUDING REMARKS

Black hole accretion discs and jets with $3\dot{M}_{\mathrm{E}}$ and $15\dot{M}_{\mathrm{E}}$ have been examined by time-dependent two-dimensional radiation hydrodynamical calculations over a far distant region and a long time-scale. Starting with the initial disc based on the Shakura–Sunyaev disc model, we examined the time evolutions of the disc and the jet. As a result, the inner disc becomes geometrically thick, optically thin, and convectively unstable. The dominant radiation pressure force in the inner region of the disc accelerates the gas flow perpendicular to the equatorial plane, and high-velocity jets with 0.2–0.4c are formed along the rotational axis. In model 1 with the lower accretion rate, the initially anisotropic high-velocity jet becomes gradually isotropic flow in the distant region of $\sim 10^{11}$ cm. The mass outflow occurs through the entire outer boundary and the mass-outflow rate is large, at $\sim 10^{19}$–10^{23} g s^{-1}, but it is variable and intermittent with time; that is, the outflow switches occasionally to inflow. At the initial phase the luminosity fluctuates around $\sim 10^{40}$ erg s^{-1} by a factor of 2 and then it flares up to 4×10^{40} erg s^{-1} and again to $\sim 10^{42}$ erg s^{-1} after a time of $2.5 \times 10^5 r_{\mathrm{g}}/c$. After that the luminosity behaves like a periodic variation with a period of $\sim 2.5 \times 10^5 r_{\mathrm{g}}/c$ and an amplitude of a factor of 10.

On the other hand, the jet in model 2 with the higher accretion rate maintains its initial anisotropic shape even after the jets go far away, and the mass outflow occurs only through the polar direction. The disc luminosity and the mass-outflow rate attain their steady values of 1.3×10^{40} erg s^{-1} and 3×10^{19} g s^{-1}, respectively. These different types of behaviour of the unstable disc luminosity in model 1 and the stable disc luminosity in model 2 are interpreted in terms of the thermal instability of the slim accretion disc model. The super-Eddington model with $15\dot{M}_{\mathrm{E}}$ promises to explain the small collimation degree of the jet and the large mass-outflow rate observed in the X-ray source SS 433.

It should be noted that these conclusions are dependent on the viscosity parameter α because we examined only low-viscosity flows with $\alpha = 10^{-3}$. In the previous numerical simulations, we found that low-viscosity flow is more advantageous to form a well-collimated powerful jet than high-viscosity flow with $\alpha = 0.1$. The characteristics of the accretion flows for different α can be qualitatively explained by the role of the viscosity in the suppression of the convective instability in the accretion flows. Thick accretion discs of low viscosity ($\alpha \leqslant 0.01$) are generally convection-dominated flows (Igumenshchev & Abramowicz 1999; Stone et al. 1999; Narayan et al. 2000; Quataert & Gruzinov 2000). The convective instability results in the vortex motion of gas of different spatial scales. Convection cells stretch from the disc mid-plane to the disc surface in the inner region of the disc. The convective flow is subsonic in the mid-plane but becomes comparable to sonic speed near to the disc surface. As a result, part of the convective flow escapes from the disc as the disc wind, dissipating the energy of powerful acoustic waves produced by convection in the disc. The outflowing material originates not only from the innermost disc near the transition region between the inner advection-dominated and outer convection-dominated zones but also from the outer upper disc as the disc wind. The disc wind is incorporated into the rarefied, hot and high-velocity region and is accelerated due to the strong radiation field in the rarefied region. However, in the case of high viscosity, the strong accretion flow smoothes the convective instability and

is globally stable convectively. As a result, the powerful jet found in the low-viscosity case is not reproduced. At present, we have no clear conclusion as to which viscosity case is realized in actual black hole accretion flows. Future 3D MHD simulations of black hole accretion flows may give a decisive answer to the viscosity problem.

ACKNOWLEDGMENTS

The authors would like to thank the referee for many useful comments.

REFERENCES

Abramowicz M. A., Czerny B., Lasota J. P., Szuszkiewicz E., 1988, ApJ, 332, 646
Abramowicz M. A., Igumenshchev I. V., 2001, ApJ, 554, L53
Balbus S. A., Hawley J. F., 2003, in Falgarone E., Passot T., eds, Turbulence and Magnetic Fields in Astrophysics, Lecture Notes in Physics. Springer, Berlin, Vol. 614, p. 329
Blandford R. D., Begelman M. C., 1999, MNRAS, 303, L1
Eggum G. E., Coroniti F. V., Katz J. I., 1985, ApJ, 298, L41
Eggum G. E., Coroniti F. V., Katz J. I., 1988, ApJ, 330, 142
Fukue J., 1982, PASJ, 34, 163
Hawley J. F., Balbus S. A., 2002, ApJ, 573, 738
Honma F., Matsumoto R., Kato S., 1991, PASJ, 43, 147
Igumenshchev I. V., Abramowicz M. A., 1999, MNRAS, 303, 309
Kato S., Fukue J., Mineshige S., 1998, Black Hole Accretion Discs. Kyoto Univ. Press, Kyoto
King A. R., Begelman M. C., 1999, ApJ, 519, L169
Kley W., 1989, A&A, 208, 98
Kotani T., Kawai N., Matsuoka M., Brinkmann W., 1996, PASJ, 48, 619
Levermore C. D., Pomraning G. C., 1981, ApJ, 248, 321
Lin D. N. C., Papaloizou J. C. B., 1985, in Black D. C., Mathews M. S., eds, Protostars and Planets. Vol. 2, p. 981, Univ. Arizona Press, Tucson
Lynden-Bell D., 1978, Phys. Scr., 17, 185
Narayan R., Igumenshchev I. V., Abramowicz M. A., 2000, ApJ, 539, 798
Okuda T., 2002, PASJ, 54, 253
Okuda T., Fujita M., Sakashita S., 1997, PASJ, 49, 679
Paczynsky B., Wiita P. J., 1980, A&A, 88, 23
Papaloizou J. C. B., Stanley G. Q. G., 1986, MNRAS, 220, 593
Pringle J. E., Rees M. J., 1972, A&A, 21, 1
Quataert E., Gruzinov A., 2000, ApJ, 539, 809
Shakura N. I., Sunyaev R. A., 1973, A&A, 24, 337
Shibata K., Uchida Y., 1986, PASJ, 38, 631
Stone J. M., Pringle J. E., 2001, MNRAS, 322, 461
Stone J. M., Pringle J. E., Begelman M. C., 1999, MNRAS, 310, 1002
Szuszkiewicz E., Miller J. C., 1998, MNRAS, 298, 888
Teresi V., Molteni D., Toscano E., 2004, MNRAS, 348, 361

This paper has been typeset from a TEX/LATEX file prepared by the author.